Modeling and validation of chemical vapor deposition of tungsten for tungsten fiber reinforced tungsten composites

L. Raumann[a], J.W. Coenen[a], J. Riesch[b], Y. Mao[a], H. Gietl[b], T. Höschen[b], Ch. Linsmeier[a], O. Guillon[a]

[a]*Forschungszentrum Jülich GmbH, Institute for Energy and Climate Research, 52428 Jülich*[1]
[b]*Max-Planck-Institute for Plasma Physics, 85748 Garching b. München*

Abstract

Tungsten is the most promising first wall material for nuclear fusion reactors. One disadvantage, however, is its intrinsic brittleness. Therefore tungsten fiber reinforced tungsten (W_f/W) is developed for extrinsic toughening. W_f/W can be produced by chemical vapor deposition (CVD), e.g. by reducing WF_6 with H_2 using heated W-fibers as substrate. However, it still needs to be optimized regarding relative density and fiber volume fraction. The decisive factor is the tungsten deposition rate, which depends on the temperature and the partial pressures. For this dependence, however, there are controversial results in the literature. In this article a new rate equation is presented, in which different literature equations are partially adapted and combined. It adjusts the WF_6 reaction order between one and zero, depending on the temperature and the H_2 and WF_6 partial pressure. For validation, a simplified experimental setup with a single fiber was designed, which provides very well defined boundary conditions while varying the CVD process parameters heating temperature, pressure, gas flow rate and gas inlet composition. The experimental runs were simulated with COMSOL Multiphysics. The model was successfully validated by measurements of the WF_6 consumption rates (< 2 to $100\,\%$), deposited tungsten masses and spatially high-resolved tungsten deposition rates.

Keywords: chemical vapor deposition, tungsten hexafluoride, rate equation, experiment, modeling, comsol

---

[1]Partner in the Trilateral Euregio Cluster.

Nomenclature

i, j Placeholder for species (WF_6, H_2, HF or W)

D_{ij} Binary diffusion coefficient [$m^2\,s^{-1}$]
$D_{eff,i}$ Effective diffusion coefficient [$m^2\,s^{-1}$]
E_A Activation energy [$J\,mol^{-1}$]
$k_{0,1,2}$ Constants for deposition rate equation [$m\,s^{-1}\,Pa^{-(n+1/2)}$]
k_B Boltzmann constant [1.381×10^{-23} J K^{-1}]
M_i Molar mass [$g\,mol^{-1}$]
Δm_W Deposited mass of W [g]
N Number of gas species [-]
n Reaction order
P_{tot} Total pressure [Pa]
p_i Partial pressure [Pa]
R Gas constant [8.314 $J\,mol^{-1}\,K^{-1}$]
R_W Deposition rate of W[$m\,s^{-1}$]
R_{exp} Experimental R_W [$m\,s^{-1}$]
R_{sim} Simulated R_W [$m\,s^{-1}$]
$R_{WF_6 dep.}$ R_W, dependent on p_{WF_6} [$m\,s^{-1}$]
$R_{WF_6 indep.}$ R_W, independent on p_{WF_6} [$m\,s^{-1}$]
S Reactive sticking coefficient [-]
T Temperature [K]
T_H Heater temperature [K]
T^* Reduced temperature $= k_B T / \epsilon_{ij}$ [-]
Δt Deposition duration [s]
U_{WF_6} Consumption rate of WF_6^{-}
$\dot{V}_i$ Volume flow rate [sccm]
x_i Mole fraction [-]

ϵ_{ij} Lennard-Jones potential parameter [J]
ρ_i^0 Standard density [g/cm^3]
σ_{ij} Collision diameter [m]
Ω Collision integral [-]

1. Introduction and motivation

The development of high-performance materials is essential for revolutionary future energy systems. For example, dealing with the enormous nuclear fusion power is one of the ultimate challenges in the design of a fusion power plant [1, 2, 3]. In the current designs, the fusion ash and other plasma contaminants are diverted out of the fusion vessel by divertors, which are the plasma facing components that must withstand the most extreme conditions. For a cost-efficient fusion power plant, the divertor material must provide reasonable operational lifetime despite enormous heat and particle fluxes, high-energy neutron bombardment, plasma erosion and thermal cycling [4]. In addition, the material is required to have a high thermal conductivity, should not produce long-living radioisotopes due to transmutation, and should not trap much hydrogen. Pure tungsten (W) is currently the main candidate material as it best meets these requirements. A major concern, however, is its intrinsic brittleness and its susceptibility to further embrittlement while exposed to neutron bombardment and overheating [5].

To overcome this disadvantage, tungsten fiber-reinforced tungsten (W_f/W) is currently being developed. Potassium doped drawn W fibers are coated by an Y_2O_3 interface and afterwards embedded into a W matrix. The interface allows for several crack dissipating mechanisms that lead to a pseudo-ductile composite behavior, even for a brittle matrix and brittle fibers – similar to fiber reinforced ceramics. Two different production routes are developed [5]. On the one hand, randomly orientated W short fibers are mixed with a W powder and sintered under high temperature and pressure [6, 7, 8]. On the other hand, arranged long fibers are used as a substrate for a chemical vapor deposition (CVD) process [9, 10, 11]. The main advantages of the latter route are significantly lower production temperatures, having no mechanical impact during fabrication, and an enhanced fiber reinforcement due to the allowance for purposefully fiber positioning. However, the process is more complex and a fully dense composite with a sufficiently high fiber volume fraction (30 - 40%) could not be achieved yet. During deposition, the process gas needs free access to all growing surfaces as long as possible. Otherwise, if the growing matrix seals open domains too early, pores will remain, as it happened in the W_f/W composite shown in Figure 1. These pores weaken the mechanical properties and the thermal conductivity. A deep process understanding is necessary to optimize the relative W_f/W density via the CVD process parameters and via the geometric fiber setup. For achieving this understanding, a CVD model is currently being developed.

This article presents the first development step of this model, which focuses on the influence of the CVD process parameters on the W deposition rate. The article starts with a review about the CVD of W and its reaction kinetics, pointing out the still open questions. In the next sections, a new experimental design and a new model for the CVD of W are described. The simulation results are validated regarding the W deposition rate, the deposited mass and the WF_6 consumption. Finally, it is shown that the proposed solution is not only able to explain the results of this study but also to explain the apparent controversies found in the literature.
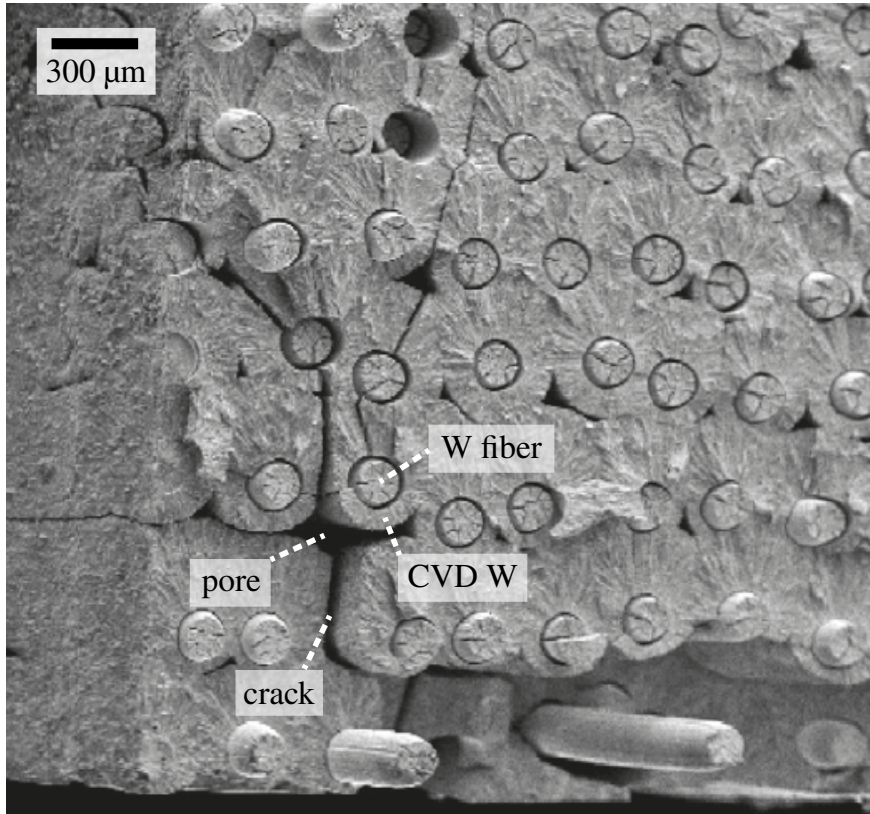
Figure 1: Fracture surface of a W_f/W sample after a charpy impact test at room temperature with a crack through a large pore [10].

2. CVD of W

CVD of W by reducing WF_6 with H_2 has several specific advantages, among them that the deposition already takes place at low temperatures, starting at about $550\,K$, and that it leads to very pure W [12]. In addition, the process is already used in microelectronics production, e.g. for metallization in Ultra Large Scale Integration (ULSI) technology [13, 14, 15, 16, 17]. Therefore, the precursors are available in large quantities, technically sufficiently pure. The net reaction for reducing WF_6 with H_2 is described by Equation 1.

$$WF_6 + 3\,H_2 \longrightarrow W(s) + 6\,HF \tag{1}$$
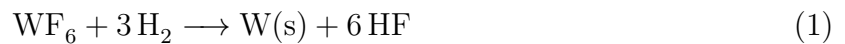
and can be divided into the following reaction steps [18]:

1. Adsorption of WF_6 and H_2 on the reaction surface
2. Stepwise dissociation of WF_6 and H_2 to W, F and H
3. Reaction of H and F to HF from the reaction surface
4. Desorption of HF

Between 1970 and 2000, many experimental studies were conducted to identify an equation for the rate-limiting reaction step [18 – 24, 27 – 29], aiming for the prediction of the overall

W deposition rate R_W. As a result, Equation 2 was found and widely accepted.

$$R_W = k_0 \, exp\left(-\frac{E_A}{RT}\right) [p_{H_2}]^{1/2}[p_{WF_6}]^n \qquad (2)$$

with the symbols explained in the section Nomenclature.

Simplified rate equations, such as the one above, have the advantage of being able to predict R_W with a relatively small amount of input data. Once the semi-empirical constants E_A, k_0 and n are known, (theoretically) only T, p_{H_2} and p_{WF_6} are needed. Thus, the efforts to find reasonable values for E_A, k_0 and n were high. However, especially the search for the value of n led to a controversial discussion: Mostly it is stated that n is zero [19, 20, 21, 22] or that it is zero as long as there is sufficient WF_6 [23, 24], with the H_2 dissociation being the rate-limiting step. For this case, several authors used an Arrhenius plot ($\ln(R_W)$ vs. $1/T$) to obtain E_A and k_0, as listed in Table 1.

Table 1: E_A and k_0 from different publications. The k_0 unit conversion is based on a W density $\rho_{W,bulk}$ of 19.25 g/cm^3 [25, 26])

E_A [kJ/mol]	k_0 [$\times 10^{-6}$ Pa$^{-1/2}$m/s]	k_0 [Pa$^{-1/2}$mol/m^2/s]	
67.0	15.4 ± N.A.	1.57 ± N.A.	[23]
69.0	16.3 ± 4.8	1.70 ± 0.49	[19]
73.0	68.0 ± N.A.	6.93 ± N.A.	[21]

On the other hand, Van de Putte et al. [27] observed, $n = 1/6$ for low p_{WF_6} and $n = 0$ for high p_{WF_6}, within the same experimental setup for a fixed T and two different similar total pressures P_{tot}. Bryant and Oosterlaken et al. observed n being 1/6 [28, 18], whereas Oosterlaken et al. measured p_i in situ 17 mm above the reaction surface via laser Raman scattering.

However, McInerney et al. proposed $n = 1$ or $n = 1/6$ [29] depending on the WF_6 surface concentration. They investigated R_W within nano-trenches for different trench aspect-ratios, T and WF_6 flow rates. Further, they found a way to express n as a function of R_W and the reactive sticking coefficient S, without a need for the near-surface p_{WF_6}. Since the trench widths were smaller than the free mean path of the WF_6 gas molecules, the WF_6 flow into the trench was simulated under consideration of geometric view factors, which took into account that the trench walls partially shaded the adsorption sites. The guess for S was refined with transient simulations iteratively, until the final R_W-profiles, within the trenches, matched to experimental scanning electron microscopy (SEM) results. They concluded that the WF_6 adsorption limits the rate if the WF_6 surface concentration is very low ($n = 1$), and that HF desorption limits the rate if the surface is saturated with WF_6 ($n = 1/6$).

On the other hand, Creighton suggested that HF desorption is very unlikely the rate-limiting step as it happens very fast and with a low activation energy [30]. Creighton also observed a decrease in R_W for a p_{WF_6} above a certain threshold, which can only be described

with a negative n. Further, Creighton reported that if the ratio of H_2 to WF_6 continues to decrease, the R_W can become zero or even negative due to etching of W atoms caused by WF_x sub-fluoride desorption. Finally, Creighton suggested that the experimentally often observed zeroth order of n is nothing else than the transition from a positive n to a negative n. However, Creighton was not able to describe the observed deposition rates quantitatively.

Arora and Pollard derived a 1D model using statistical mechanics, transition state theory and bond dissociation enthalpies, to identify the major reaction pathways and rate constants [31]. Taking into account 21 sub-species and 65 surface processes, they reported the rate-limiting steps to be either the conversion of WF_4 to WF_3, or the removal of adsorbed F by H_2.

With better computers it became feasible to enhance the simplified or even detailed rate equations with fluid dynamics and heat transfer simulations, including reactor geometries. Thus, more realistic inner surface conditions could be calculated based on the external process conditions, leading to a better matching and understanding. Kleijn et al. implemented Equation 2 with $n = 0$ in the commercial fluid flow simulator Phoenics for the optimization of CVD processes for blanket W depositions [24].

Later on, Kleijn's group implemented the detailed rate equations from Arora and Pollard [15, 16, 17]. Their approach of combining the Arora model with CVD reactor simulations allowed for describing the selectivity loss of the W deposition. The term selectivity loss refers to the phenomena that W deposits, at high pressure and high temperature, not only on metallic but also on oxidic surfaces, which needs to be avoided for the ULSI circuit production. In addition, it covers the negative n for WF_6:H_2 over-stoichiometry as observed experimentally by Creighton [30]. However, it does not result in $n = 0$, as experimentally observed for changing p_{WF_6} over 2-3 orders of magnitude.

In summary, many different observations and conclusions have been made regarding the tungsten deposition kinetics, still leaving the open question: Which model, which rate equations and which values for n, E_A and $k_{0,1,...}$ should be used? To find the answer, new W deposition experiments with very carefully monitored process conditions were performed, which are described in the next section.

3. Experimental procedure

The goal of the experimental design was to get R_W results for a wide range of process parameters (heater temperature T_H, total pressure P_{tot}, and gas flow rates $\dot{V}_i^{inlet}$) with high precision and spatial resolution. In addition, a large range of U_{WF_6} values (<5 to 100%) should be obtainable. The experimental setup is shown in Figure 2.

Each sample was a unit consisting of a stainless steel (EN 1.4571) tube, a coaxially mounted W fiber, and two fiber holders (EN 1.4571). The W fiber had an outer diameter (OD) of $150\,\mu$m, while the tube had an OD of $10\,$mm and a wall thickness of $1\,$mm. Both had a length of $220\,$mm. For each process parameter set, a new uncoated sample-unit was connected to the vacuum system of the CVD chamber via swagelok compression fittings. Secondly, for high thermal contacts, cylindric heaters were clamped around half shells filling up the space to the tube. The half shells (EN 1.4571) had a inner diameter of $10\,$mm, an
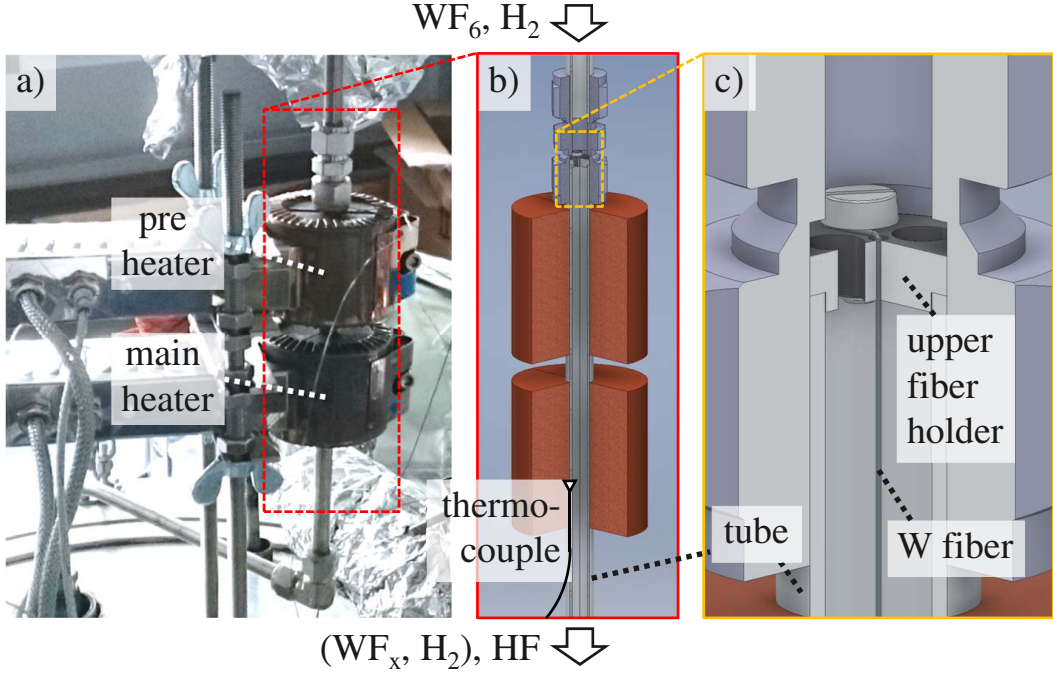
Figure 2: Experimental setup for the CVD of W inside a steel tube and on a coaxially aligned W fiber. a) Photograph, b) 3/4 slice of the sample-unit and the half shells allowing for thermal contact from the heaters to the tube, c) Close-up of the upper fiber holder.

OD of 48 mm, a lengths of 53 mm and an axial distance of 13 mm. Thus, each sample unit can be considered as a "hot-wall reactor" heated from the outside along two zones. The first and upper zone acted as a pre-heating zone (533 K), while in the second zone T_H was varied during the parameter study. The thermocouple, used for controlling T_H (Figure 2, b, $\triangledown$-symbol), was inserted tightly into a groove that was cut into the inside of the main heater filler material (14 mm long, from the bottom).

During heating up to thermal equilibrium, $\dot{V}_{H_2}^{inlet}$ and P_{tot} were set to values as in the corresponding following experimental run. Additionally, only during heating up, an Ar gas flow $(= 2 \cdot \dot{V}_{WF_6}^{inlet})$ was applied. In this way, T_H did not change significantly by switching from Ar to WF_6, which started the deposition. The used process parameters are listed in Table 2.

The W deposition thicknesses were evaluated based on optical microscopy. Each coated fiber was carefully taken out of the tube being still fixed to its upper holder, in order to preserve the axial position as mounted inside of the tube. The fibers were captured in one piece against a bright background. The inside coated tubes were filled with embedding material, sliced lengthwise and polished down to the half before capturing. A python script was written to measure the W thickness for each pixel column along pictures with a height of > 700 pixel, a lengths of $> 100\,000$ pixel and a resolution of $1.36\,\mu$m/pixel. An example resulting from this thickness measurement is provided in Figure 3. The complete experimental results will be shown comprehensively after the model description, while being compared to the simulation results.

Table 2: Measured and time-averaged CVD process parameters. The boldly formatted numbers belong to a series, where the respective parameter in the column head was varied while the other process parameters were kept constant, if possible.

|	Process parameters				Further calculated parameters		
ID	T_H [K]	$\dot{V}_{H_2}^{inlet}$ [sccm]	$\dot{V}_{WF_6}^{inlet}$ [sccm]	P_{tot} [kPa]	$p_{H_2}^{inlet}$ [kPa]	$p_{WF_6}^{inlet}$ [kPa]	$\dot{V}_{tot}^{inlet}$ [sccm]
1100	**773**	208	25	10.0	8.91	1.09	233
1086	**873**	208	26	**10.1**	9.00	1.10	233
1101	**913**	208	26	10.0	8.88	1.12	**234**
1090	873	**808**	50	9.93	9.35	0.58	858
1091	873	**407**	**51**	10.0	8.90	1.11	458
1092	873	**208**	51	10.0	8.05	1.96	258
1093	873	407	**100**	10.0	8.02	1.98	507
1088	873	208	25	**2.50**	2.23	0.27	233
1089	873	208	26	**0.60**	0.54	0.07	234
1096	773	800	200	3.12	**2.49**	0.62	1000
1095	773	889	111	5.61	**4.99**	0.62	1000
1097	773	941	59	10.6	**10.0**	**0.63**	1000
1098	773	980	21	10.2	10.0	**0.21**	1000
1099	773	800	200	12.5	10.0	**2.50**	1000
1094	913	808	101	9.96	8.85	1.11	**909**
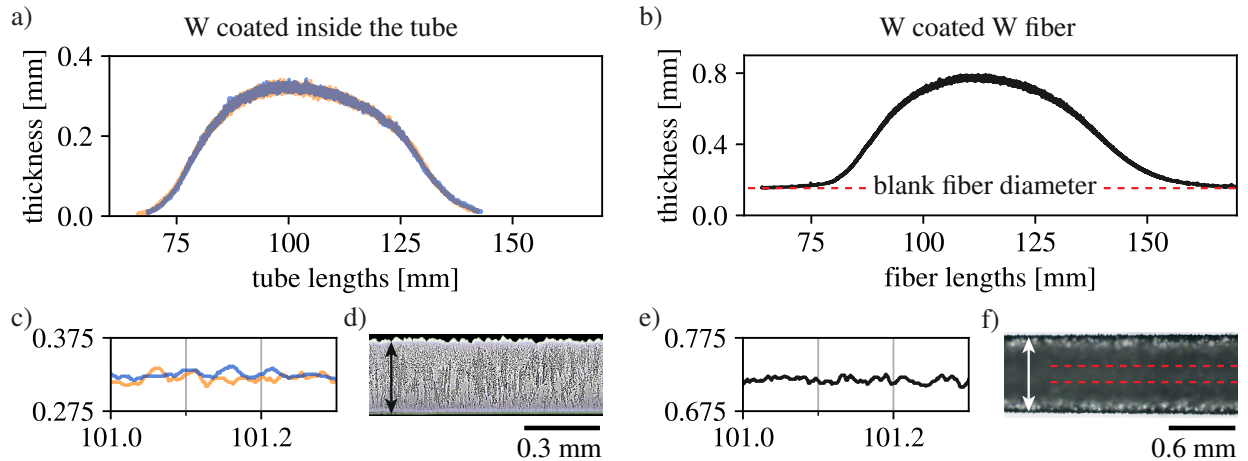
Figure 3: Example for the coating thickness measurements (here #1092). a) Inner tube coating thickness with two overlaid curves for each side of the sliced tube. b) Coated fiber thickness. c, e) Zoomed sections of the plots above, with evenly scaled axes to show that the graphs resolve the surface grain structure of the CVD-W. The envelopes of the graphs are the major part of the error bars of R_{exp}. d, f) Image sections near the thickness maxima.

The total W mass gain $\Delta m_{W,exp}$ was obtained by weighting each sample-unit (tube, fiber, fiber holders), together with its swagelok nuts and cutting rings, before and after deposition.

The experimental WF_6 conversion rate $U_{WF_6,exp}$ was estimated according to Equation 3. $U_{WF_6,exp}$ equals the converted WF_6 mass divided by the total WF_6 mass, which was sent into the heated tube.

$$U_{WF_6,exp} = \frac{\text{converted } m_{WF_6}}{\text{sent in } m_{WF_6}} \cong \frac{\Delta m_{W,exp} \cdot \dfrac{M_{WF_6}}{M_W}}{\dot{V}_{WF_6}^{inlet} \cdot \Delta t \cdot \rho_{WF_6}^0} \tag{3}$$

The converted WF_6 mass was estimated via $\Delta m_{W,exp}$ and the mol ratio of WF_6 and W. The total amount of sent in WF_6 mass was calculated via $\dot{V}_{WF_6}^{inlet}$ multiplied by the deposition duration Δt and the standard density of gaseous WF_6 (12.4 kg/m^3 [32]).

The T distributions inside of the samples, where the W deposition took place, have the largest impact on R_W, and are therefore crucial for the presented study. Since it is not possible to know them just from a single value (T_H, controlled by a single fixed thermocouple on the outside of the tube), an additional modified setup has been designed to measure the inner T-profiles as a function of the process parameters (T_H, P_{tot}, $\dot{V}_i^{inlet}$). In this setup, graphite greased thermocouples with an OD of 0.5 mm were moved along the inner of two stainless steel capillaries with an inner diameter of 0.6 mm. One capillary was tightly fitted into a round groove, which had been eroded into the inner tube surface. The other one was placed in the tube axis replacing the W fiber (Figure 4). The wall thickness of the capillaries was chosen at only 0.1 mm to measure the T closely, but still feasibly, below the reaction surface. The fixed capillaries and movable thermocouples penetrated the "L"-connection at the bottom (Figure 2, a). Below, the thermocouples were clamped both to the same digital calliper. T-profiles were acquired by opening the calliper in 3-4 mm steps manually, and thus pulling the tips out, while the T and positional values were recorded by a script.
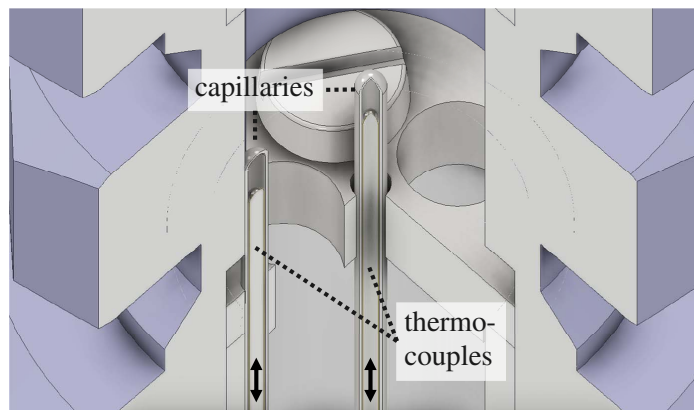

Figure 4: 3/4 slice of the modified sample head to measure the inner T with a high spatial resolution.

All T profile measurements were carried out subsequently, using the same described modified setup. After moving the thermocouple tips, it took for each single data point

between five and nine seconds until the thermal equilibrium was reached and the data recorded. Therefore, in order to keep the influence of the growing W on the T low, only the 8 out of 15 experimental parameter sets, which lead to the lowest deposition rates, were investigated. These involved mainly low T_H. Additionally, the complete T_H range as in the deposition experiments (up to of 913 K) was tested with different P_{tot} and $\dot{V}_{H_2}^{inlet}$ values, before using WF_6, in order to have also sufficient data for the heat model validation with respect to the high T_H values.

4. Model description

The new model for CVD of W is developed utilizing the finite element method (FEM) software COMSOL Multiphysics [33]. It considers the complex coupling of transport phenomena, chemical reaction kinetics and solid domain growth. The simulation boundaries of the 2D axial-symmetric model are shown in Figure 5. An overview of the used material and species properties is provided in the appendix in Table 7. It was verified with an extra 3D fluid dynamic simulation of the inlet that the upper fiber holder (Figure 2c) was far enough away to not violate the 2D axial-symmetry within the 2D simulation-boundaries.
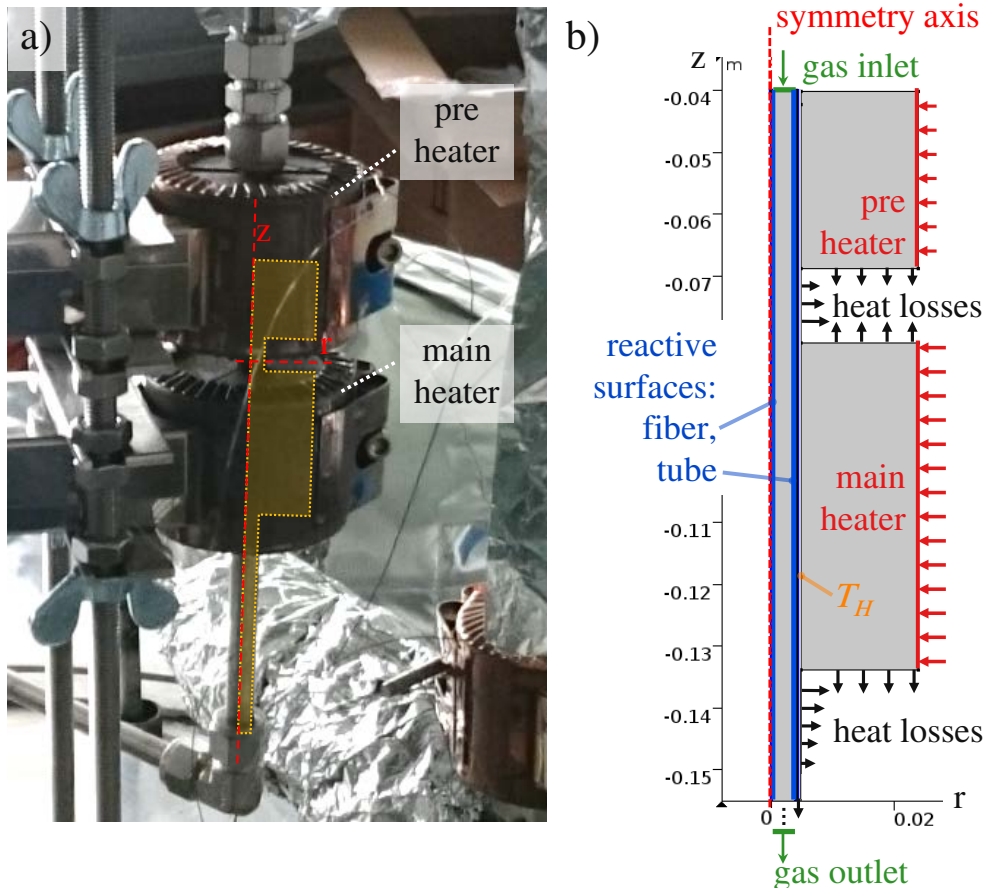

Figure 5: a) Location of the model within the experimental setup. b) Sketch of the model boundaries.

10

4.1. Fluid dynamics

The gas mixtures are considered as contina. For the mono-species H_2, WF_6, and HF, the heat capacity was fitted to tabulated data from Barin (Ed.) [35], while the gas density, dynamic viscosity, and thermal conductivity are calculated from the Lennard-Jones parameters ϵ/K_B, σ and μ_D as in [36]. The spatially resolved gas mixture properties are calculated by COMSOL Multiphysics [33], based on the mono-species values and the local mass fractions. Similar equations can be found in [24]. Further, the gas flow was assumed to be laminar. This assumption was verified as final step again, by calculating via Equation 4 the Reynolds number Re to be $\ll 2000$, as described in [34].

$$Re = \frac{dv\rho}{\eta} \tag{4}$$

with the inner tube diameter $d = 8\,\text{mm}$, and the cross-sectional-averaged gas velocity v, the gas mixture density ρ and dynamic viscosity η taken for each ID from the simulation results.

The ordinary molecular diffusion (concentration gradient driven) is modelled following the Wilke-approximation [37]. Fairbanks and Wilke proposed that the effective diffusion coefficients $D_{eff,i}$ can be described with Equation 5.

$$D_{eff,i} = (1 - x_i) \left(\sum_{i=1, j \neq i}^{N} \frac{x_j}{D_{ij}} \right)^{-1} \tag{5}$$

The binary diffusion coefficient D_{ij} can be estimated via the kinetic gas theory [36]. Kuijlaars specified the following empirical formula for D_{ij} [15] by using the empirical correction from Wilke and Lee [38]:

$$D_{ij} = (6.77 - k_M 0.0492)\, k_M \frac{T^{3/2} \times 10^{-4}}{P_{tot} \sigma_{ij}^2\, \Omega(T_{ij}^*)} \tag{6}$$

with $k_M = \sqrt{\frac{1}{M_i} + \frac{1}{M_j}}$ and with $\Omega(T_{ij}^*)$ being the collision integral, which is a stepwise defined function of the reduced temperature $T^* = k_B T/\epsilon_{ij}$, tabulated in e.g. [36]. To reduce the needed model input and the computational effort, $\Omega_{ij}(T^*)$ was fitted as a function of T for each species pair in the mixture of H_2, WF_6 and HF. These fits were inserted into Equation 6 and fitted again to simplified functions depending only on T and P_{tot}. The result of this procedure is shown in Equation 7. The error of using Equation 7 instead of Equation 6 is less than 0.64% for T between 300 and 1200 K.

$$D_{ij} = \sum_{k=0}^{2} \frac{a_k \cdot T^k}{P_{tot}} \tag{7}$$

with a_0, a_1, a_2 listed in Table 3.

In addition, it was tested to describe the ordinary diffusion using the more computational costly Stefan-Maxwell formulation [39] instead of the Wilke-approximation. Further, also thermal diffusion [36] was included. Both attempts resulted, for the present experimental

11

Table 3: Polynomials a_0, a_1 and a_2 to calculate D_{ij} according to Equation 7.

ij	a_0 [Pa m^{2}s^{-1}]	a_1 [Pa K^{-1}m^{2}s^{-1}]	a_2 [Pa K^{-2}m^{2}s^{-1}]
H$_2$ WF$_6$	-2.518	1.521×10^{-2}	1.459×10^{-5}
HF WF$_6$	-6.384×10^{-1}	2.922×10^{-3}	5.583×10^{-6}
H$_2$ HF	-4.832	2.885×10^{-2}	3.498×10^{-5}

setup, in a negligible difference compared to using only the Wilke-approximation as described above. The reason is that this setup is dominated by convection in combination with only very small T gradients perpendicular to the inner surfaces.

4.2. Heat transfer

COMSOL Multiphysics in-built functions were used for simulating thermal conduction, convection and radiation [33]. The heater temperature T_H was not simulated directly, but instead a simulated heating power was controlled to match T_H at the same position, at which the controlling thermocouple was placed in the experiment. This was necessary to simulate the convective cooling of the inner surfaces by the inflowing gas. The simulations were conducted transiently, whereby the growing W coating was taken into account by a deforming mesh. The deposited W changes the effective heat conductivity, especially in axial direction. This effect leads to an increasing heating power during the deposition process, which was observed in the simulation as well as experimentally.

The real values of the thermal losses to the surrounding, and especially of the gap conductance between the outside of the steel tubes and the inside of the clamped half shells, are not accessible for validation. However, their values become narrowed down by many experimental results, which are accessible. For example, a higher gap conductance increases the maximum and the broadness of the T-profiles and thus increases also the WF$_6$ consumption. Further, a higher gap conductance reduces the influence of the convective gas cooling and therefore shifts the axial position of the W coating on the fiber towards the center of the heating zone.

Therefore, firstly the thermal losses and the gap conductance were chosen to satisfy 19 sets of experimentally recorded T-profiles (at tube and fiber position). The T-profiles include measurements without gas flow or with only H$_2$ flow for different T_H and P_{tot}. They include further the measurements for the process parameters as in Table 2 for #1089, #1091, #1095 − 1100 (lower R_{W}). Secondly, the T-profiles were modelled for the missing IDs with just the process parameters as changing input. Finally, the values for the thermal losses and the gap conductance were refined to satisfy additionally the experimental data of all 15 WF$_6$ consumption rates and axial positions of the W coating thickness peaks along the fibers.

It was found that the gap conductance has to increase with T_H, which is meaningful, since a higher thermal expansion leads to a higher contact pressure.

4.3. Chemistry and rate equations

Negative n are of no concern for the synthesis of W_f/W, since the H_2 to WF_6 ratio is kept > 3. In addition, the avoidance of a selectivity loss does not need to be considered for W_f/W. Therefore, it was decided to neglect detailed sub-reactions and sub-species, such as WF_x with $x < 6$. Gas bulk reactions were neglected as well. Instead, fast-solving simplified rate equations (8, 8a and 8b) were used to describe the chemical reactions at the surface. The finding of Equation 8 is the major outcome of the presented article and will be validated and discussed in the following sections. Equation 8a was used as suggested by McInerney et al. [29], since no further adjustment was necessary. Equation 8b, however, was adjusted in its semi-empirical constants E_A and k_0 with respect to the experimental and simulated data from this work. The adjusting procedure is described in the last section, before the summary. This section order was chosen, because the procedure, which inhabits several complicated iterative steps, is easier to understand after the experimental and modeling results have been shown and discussed.

The species mass fluxes, towards (WF_6, H_2) and originating from (HF) the reactive surface boundaries, as shown in Figure 5, are calculated via the stoichiometry, resulting from Equation 1, in conjunction with the reaction rate (Equation 8). The heat of reaction is calculated via the thermodynamic properties of the species as listed in Table 7 in the appendix. R_{sim} (Equation 8) was smoothly set to zero starting at $p_{WF_6} < 0.3\,\mathrm{Pa}$ or $< 473\,\mathrm{K}$, to achieve faster convergence without any physical relevance for this setup.

Further simulated quantities, used for validation, were $\Delta m_{W,sim}$ and $U_{WF_6,sim}$. Since the simulated sample cannot just be weighted as the real one, $\Delta m_{W,sim}$ was obtained by multiplying the simulated deposited W volume with the density of CVD W ($19.25\,\mathrm{g/cm^3}$ [25, 26]). On the other hand, $U_{WF_6,sim}$ is simply accessible via Equation 9.

$$R_{sim} = min(R_{WF_6 indep.}, R_{WF_6 dep.}) \tag{8}$$

with $R_{WF_6 dep.}$ from Equation 8a and $R_{WF_6 indep.}$ from Equation 8b.

$$R_{WF_6 dep.} = \left(\frac{1}{k_1\, p_{WF_6}} + \frac{1}{k_2\, exp\left(\dfrac{-E_A}{RT}\right) [p_{H_2}]^{1/2} [p_{WF_6}]^{1/6}} \right)^{-1} \tag{8a}$$

with $E_A = 64\,\mathrm{kJ/mol}$, $k_1 = (32.63 \pm 2.88) \times 10^{-9}\,\mathrm{m\,s^{-1}Pa^{-1}}$ and $k_2 = (45.79 \pm 1.28) \times 10^{-7}$ $\mathrm{m\,s^{-1}Pa^{-2/3}}$, [29].

$$R_{WF_6 indep.} = k_0\, exp\left(-\frac{E_A}{RT}\right) [p_{H_2}]^{1/2} \tag{8b}$$

with $E_A = (73.7 \pm 0.9)\,\mathrm{kJ/mol}$ and $k_0 = (3.99 \pm 0.51)\,\mathrm{mol\,m^{-2}s^{-1}Pa^{-1/2}} = (38.22 \pm 4.85) \times 10^{-6}\,\mathrm{m\,s^{-1}Pa^{-1/2}}$.

$$U_{WF_6,sim} = 1 - \frac{\dot{V}^{inlet}_{WF_6,sim}\, \Delta t}{\int_0^{\Delta t} \dot{V}^{outlet}_{WF_6,sim}\, dt} \tag{9}$$

13

with $\dot{V}_{\mathrm{WF}_6,sim}^{inlet}$ constantly being equal to $\dot{V}_{\mathrm{WF}_6}^{inlet}$ (Table 2), thus no integration is necessary. And with $\dot{V}_{\mathrm{WF}_6,sim}^{outlet}$ decreasing over time, because as the W grows, the T-profiles become slightly broader. This indeed led to, depending on the process parameters, an increase of $U_{\mathrm{WF}_6,sim}$ between 0.02 and 3.3 %, from the start to the end of a deposition.

5. Results and model validation

This section will firstly provide simulation result examples as color maps within the 2D axial-symmetric geometry, followed by a detailed comparison of the simulated versus the experimental results. Figure 6 shows how the gas mixture flows in from above and is heated in the hot area where the CVD reaction takes place so that W is deposited while WF_6 and H_2 are consumed.

These kind of plots are well suited as introduction, since they help to develop a first process understanding, and to check the simulation for plausibility. However, to precisely compare the simulated and experimental results, as next step, T and R_W are plotted as lines (simulated) and as symbols (experimental) along the fiber and the inner tube surface, in z direction. Lines for p_i are included as well to overview all important quantities, which determine R_W. In Figure 7 the comparison for the $p_{\mathrm{H}_2}^{inlet}$-variation is depicted. The simulated results match very well to the experimental results. The results were averaged over Δt, except for the experimentally acquired T, which was measured only once, as described in the last part of the experimental procedure (section 3). The deposition rate R_W rises with increasing T within the main heating zone and with increasing p_{H_2}. The $\dot{V}_{tot}^{inlet}$ was chosen high, so that p_i stayed almost constant along the tube length. This was done in order to nearly rule out the influence of depletion, aiming for a modeling simplification, to start with. However, for such high $\dot{V}_{tot}^{inlet}$, thermal effects need to be considered more carefully. The different outlet pressures lead to different gas velocities. Consequently, especially on the fiber, the different gas velocities lead to different amount of convective cooling (T drop) and to an x-axis-shift of the R_W-peak. But finally, this kind of effects, which were measured experimentally, could also be correctly implemented into the model, as the results show in Figure 7, right column.

The next plot-group, Figure 8, shows the model validation for the variation of T_H. Besides the higher T_H, $\dot{V}_{tot}^{inlet}$ is significantly lowered, compared to the series, shown before. This was done, to also investigate the effect of WF_6 depletion on R_W. The lowest sub-plot row shows how p_{H_2} and p_{WF_6} decrease, while p_{HF} increases. As expected, this conversion increases with increasing T_H. As it can be seen in the left sub-plot column, for $T_H = 913\,\mathrm{K}$, R_W collapses to zero still within the hot area. This collapse leads to an intersection with the R_W curve for 873 K, since here U_{WF_6} is only 90 % so that R_W does not suffer from fully WF_6 depletion and stays, towards the end of the main-heating zone, higher than R_W for $T_H = 913\,\mathrm{K}$. This can be observed experimentally and is also covered well by the model.

Regarding R_W on the fiber, the same can be observed in the right sub-plot column, but less pronounced. The reason for this is that U_{WF_6} is slightly lower on the fiber due to a smaller surface area and due to a slightly narrower T peak, caused by the convective cooling from the incoming gas.
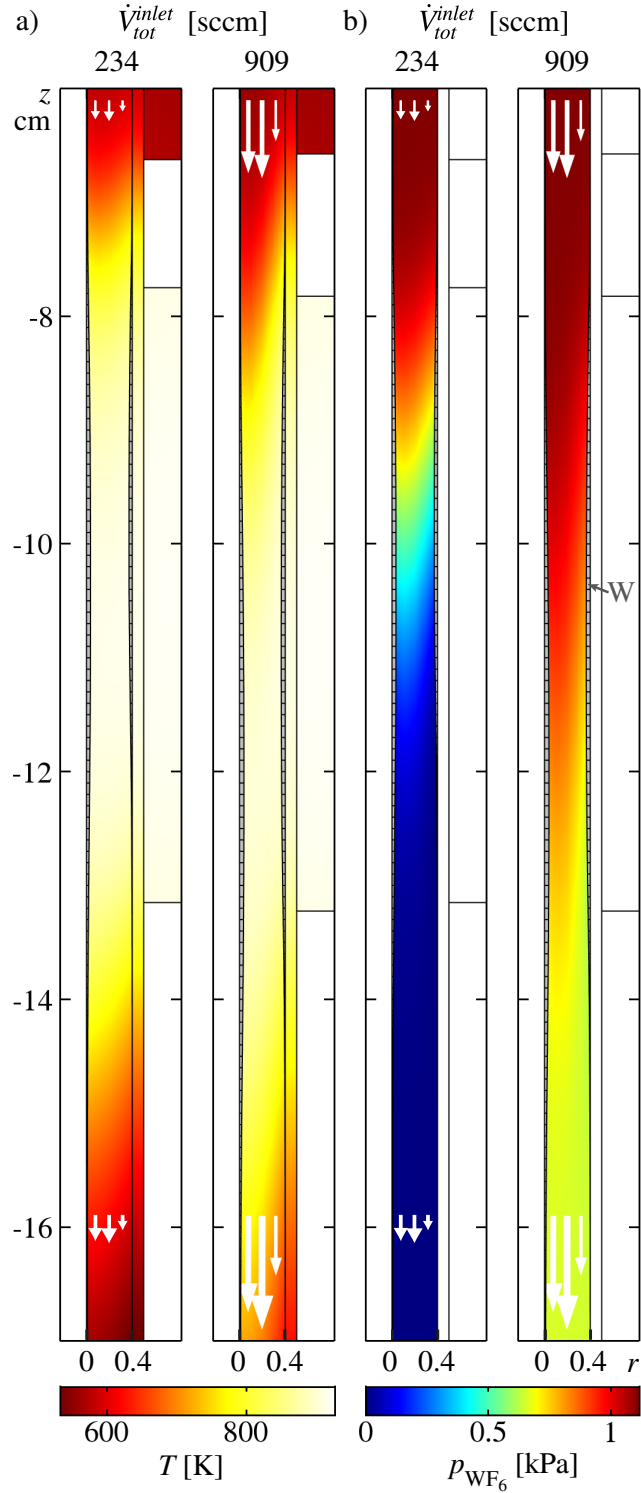
14

Figure 6: 2D simulation results in the final time step with color maps for a) T and b) p_{WF_6}, for different $\dot{V}_{tot}^{inlet}$ (#1101 and #1094). The vectors depicts the gas flow direction with the lengths being proportional to the flow rate. At the fiber surface (radius $r = 0.075$ cm) and the inner tube surface ($r = 0.4$ cm) the simulated W coatings can be seen within the hot area.
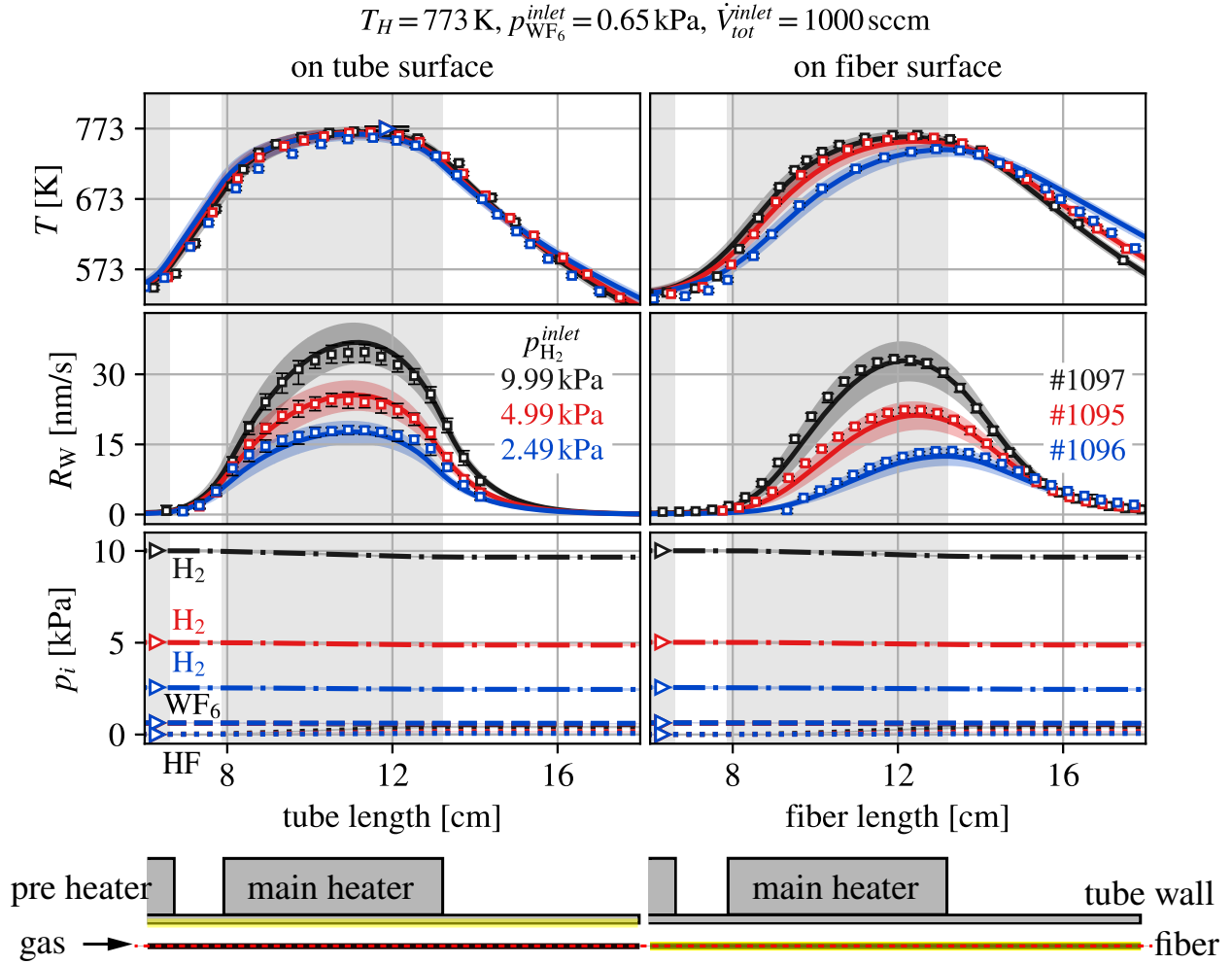
15

Figure 7: Model validation for the variation of $p_{H_2}^{inlet}$ with subplot rows for T, R_W and p_i. The left and right subplot columns show the results along the tube and fiber surface, respectively. Each color represents the data from one CVD process parameter set (same as one row in Table 2 with the corresponding ID). In the header, the constant process parameters are given. The symbols ($\square$, $\triangleright$) represent experimentally measured results, with ($\triangleright$) being data used as input for the simulation. The solid lines represent the simulated T or R_W. The dashed, dash-dotted and dotted lines represent the simulated p_{WF_6}, p_{H_2} and p_{HF}, respectively. The grey areas mark the pre and main heater positions.
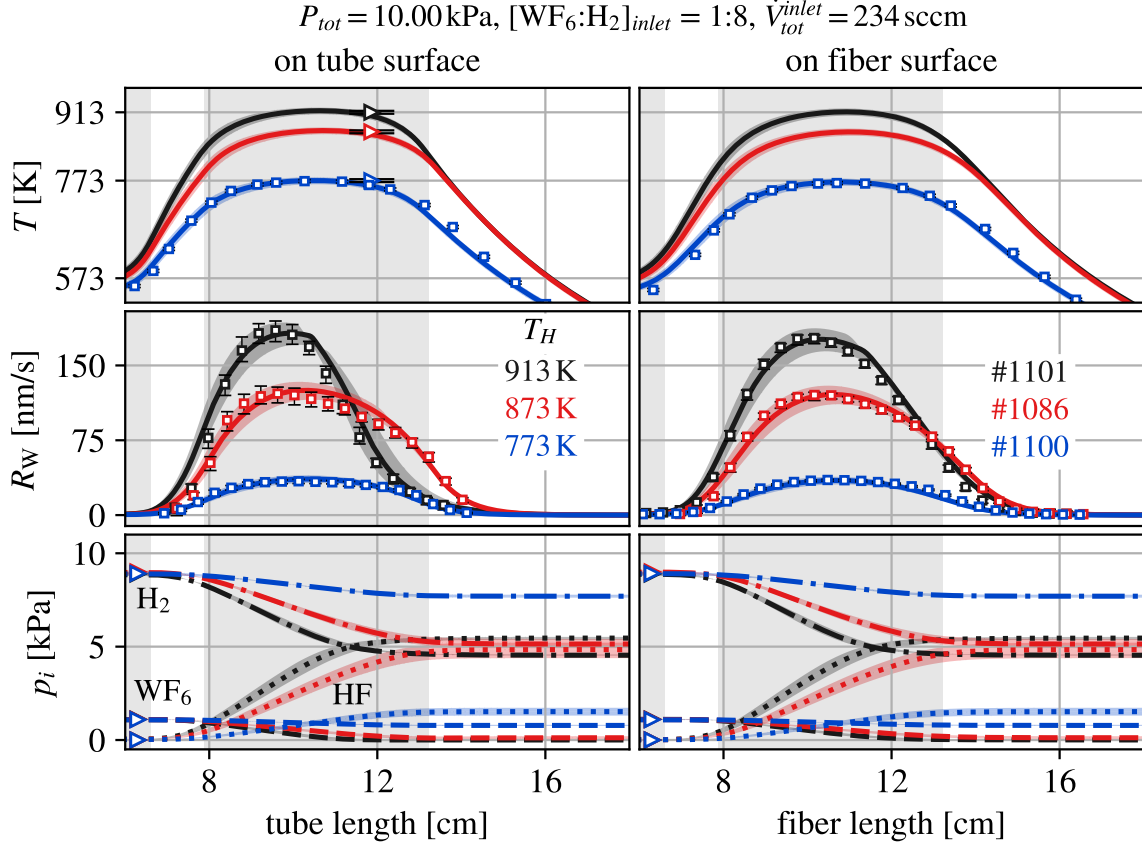
Figure 8: Model validation for the variation of the T_H. Apart from that, identical labeling to Figure 7.

The special case of the just shown R_W collapse for $T_H = 913\,\mathrm{K}$, is depicted in Figure 9a more detailed. Here, the deposition rate equations (8a,8b) are shown additionally, together with p_{WF_6}, both on/near the inner tube surface. It can be seen that $R_{WF_6 dep.}$ (Equation 8a) results in an overestimation of R_{exp} before the intersection point at x = 10.8 cm, while $R_{WF_6 indep.}$ (Equation 8b) results in an overestimation of R_{exp} after the intersection. Only by taking the minimum of both rate equations, as it is done by R_{sim} (Equation 8), the experimental results are matched well along the complete tube lengths.

The idea behind another tested parameter set was that, if more process gas is offered, the complete depletion of WF_6 should not happen for otherwise same conditions. This was proven with #1094 experimentally and in the simulation. Here, the $\dot{V}_{tot}^{inlet}$ was increased from 234 sccm to 909 sccm, for otherwise same parameters compared to #1101. The result is shown in Figure 9b. p_{WF_6} stays high in the experiment and in the simulation, indeed, and no change in the limiting rate equation takes place. Additionally, with #1094 having the highest T and $\dot{V}_{tot}^{inlet}$ combination, it can be seen that W really did not deposit outside of the samples, which would be at x-axis values > 22 cm. This is important for a correct validation of Δm_W and U_{WF_6}.
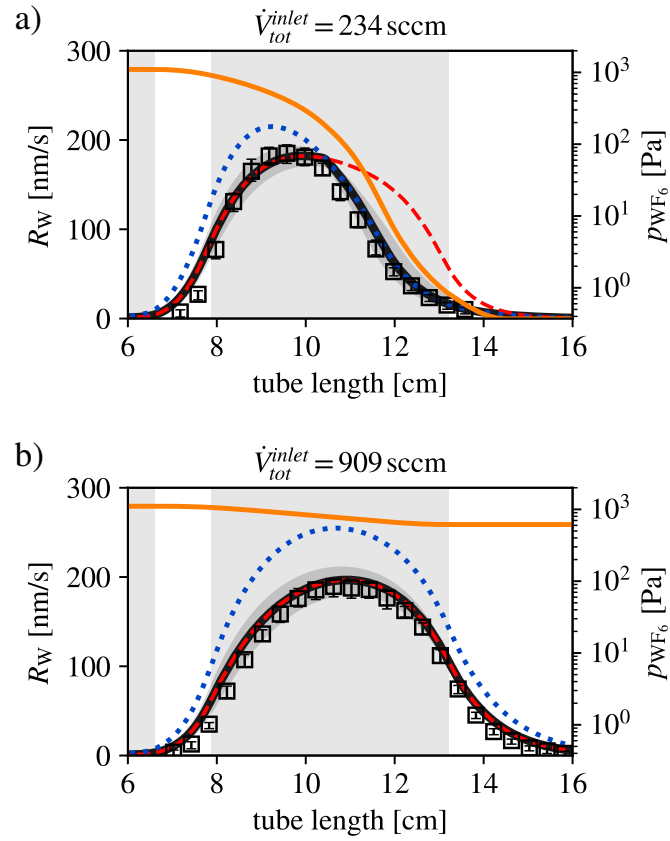
Figure 9: p_{WF_6} (——) and R_{W} at the inner tube surface versus the tube length for different $\dot{V}_{tot}^{inlet}$, with R_{exp} ($\square$) and R_{sim} (▬) following the minimum of $R_{\mathrm{WF}_6 dep.}$ (·····) and $R_{\mathrm{WF}_6 indep.}$ (----). $T = 913\,\mathrm{K}$, $P_{tot} = 10.0\,\mathrm{kPa}$, $[\mathrm{WF}_6{:}\mathrm{H}_2]_{inlet} = 1{:}8$. a) $\dot{V}_{tot}^{inlet} = 234\,\mathrm{sccm}$, #1101, b) $\dot{V}_{tot}^{inlet} = 909\,\mathrm{sccm}$, #1094. For these IDs the 2D color maps were shown in Figure 6.

Since not all 15 parameter sets (Table 2) can be discussed in detail in this article, Figure 10 provides an overview of the experimental versus the simulated results. It compares the maximal deposition rates R_{max} in the tubes and on the fibers, as well as Δm_{W}, and U_{WF_6}. $R_{sim,max}$ and $R_{exp,max}$ are very well in agreement for both, on the fiber and inside the tubes. Since R_{max} matches, the comparison of Δm_{W} gives an indication about how well the broadness of the R_{W} profiles (as in Fig. 7 – 9b) matches. Also here, the agreement is good for all process parameter sets. Finally, $U_{\mathrm{WF}_6,sim}$ (Equation 9) matches also well to $U_{\mathrm{WF}_6,exp}$ (Equation 3), validating the chemical model part, in an additional way. As conclusion, Figure 10 combines the successful validation of the experimental results regarding the in situ process parameter measurements and the post deposition optical and gravimetric measurements.
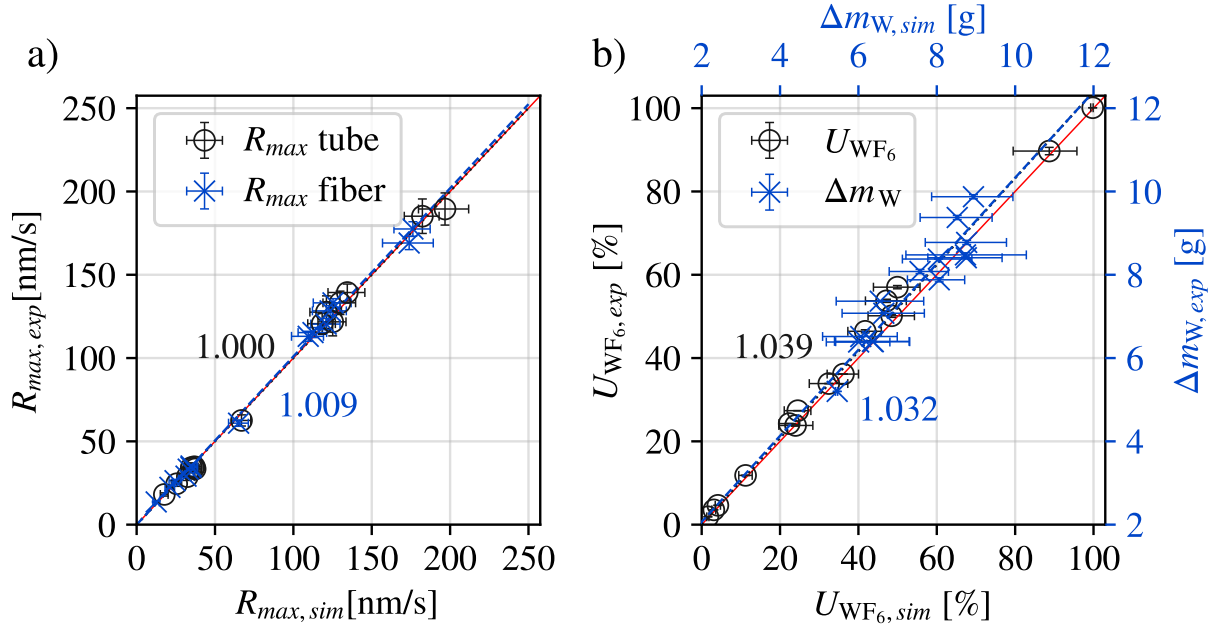

Figure 10: Overview of the comparison between experimental and simulated results for a) $R_{exp,max}$, $R_{sim,max}$, which are also tabulated in the appendix, and for b) U_{WF_6} and Δm_{W}.

6. Discussion

Besides the background motivation of W_f/W, one of the main goals of this study is to improve the common understanding of the W deposition rate and to find a simple deposition rate description that is valid for a broad parameter regime. All experiments of this study can be described successfully by using Equation 8. As next step it will be shown that this approach can even be applied to acquire a coherent description of different experimental results from literature. Even though, these results lead, on their own, to contradicting conclusions, especially regarding the p_{WF_6} dependence, as it was reviewed earlier. In Figure 11 experimental data from this study and from the literature is plotted together with calculated

results using Equation 8. As input for Equation 8, the averaged T and p_{H_2} were taken from the experimental data as described by the respective authors.
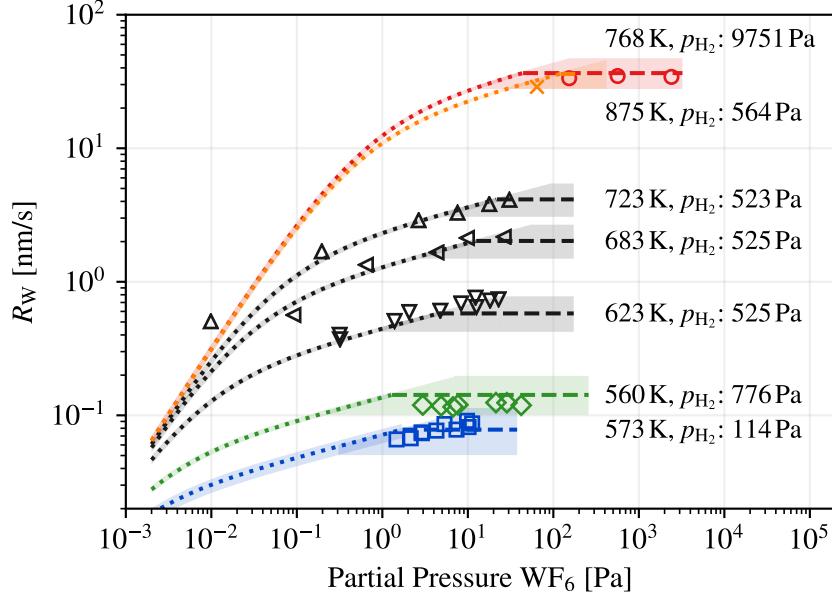

Figure 11: Lines: R_W [Equation 8], as minimum of $R_{WF_6 dep.}$ (·····) and $R_{WF_6 indep.}$ (---), vs. experimental data: ×○ this work, with $R_{max,tube}$ for #1089 (×) and #1097−1099 (○), △◁▽ Oosterlaken [18], ◇ Pauleau [20], ☐ Van der Putte [27].

Equation 8 describes the transition in the WF_6 reaction order n_{WF_6} from $1/6$ (·····), for low p_{WF_6}, to zero (---), for high p_{WF_6}. This transition point matches well to the experimental observations by Van der Putte et al. (☐) [27].

Furthermore, the experimental results of Pauleau et al. (◇) [20] show always a $n_{WF_6} = 0$, even though p_{WF_6} reaches lower values than at the transition point observed by Van der Putte et al. (☐) [27]. This is also covered by Equation 8, since the p_{WF_6} value, for which n_{WF_6} changes, is strongly depending on T. Therefore, the transition point shifts to lower p_{WF_6} in the case of lower T, as it was used by Pauleau (◇) compared to Van der Putte (☐). In addition, the reason for the higher R_W, despite the lower T, is the higher p_{H_2}.

This explains, why Pauleau et al. [20] and many others did not observe any p_{WF_6} dependence, even though partly reaching higher R_W and/or lower p_{WF_6} compared to the authors reporting a clear p_{WF_6} dependence. On the other hand, McInerney [29] and Oosterlaken [18] observed only a p_{WF_6} dependence, because most of their experiments had significantly lower p_{WF_6} and higher T. Although Oosterlaken et al. [18] reported the p_{WF_6} dependence for all their data, with this updated point of view, the up-most right data points of the series (◁, ▽) may well be reinterpreted to follow the change in rate equations. Using a rate equation being independent of p_{WF_6} down to very low p_{WF_6} of few Pascal, as suggested by Kleijn et al. and Hasper et al. [40, 41], would overestimate R_W, compared to the results of McInerney (·····), Oosterlaken (△◁▽) and Van der Putte (☐), and it would also not fit to the experimental results from this study such as #1089, and #1101 (Figure 9a). The

rate equations are limited to $p_{WF_6} < p_{H_2}/3$, because for higher p_{WF_6} there is not yet sufficient data. Further, the experimental p_{WF_6} variation of Creighton [30] is not included due unknown T and due to unusual high R_W for the reported pressure regime.

Taking into account the work by the various authors together with the new findings of this work, the overall understanding of the W deposition kinetics is proposed as following. Figure 12 shows a sketch, which is divided into four zones for the different reaction orders.
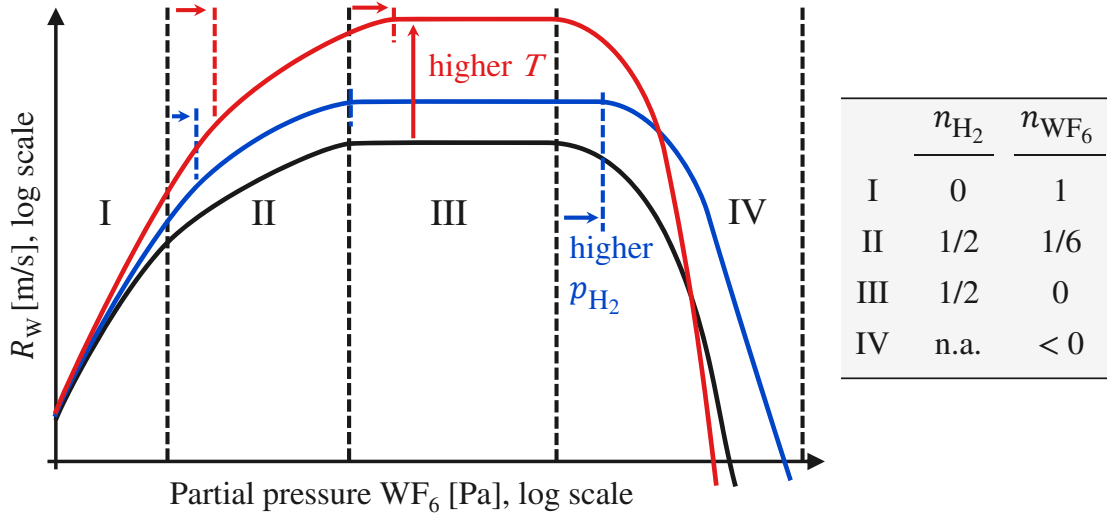

	n_{H_2}	n_{WF_6}
I	0	1
II	1/2	1/6
III	1/2	0
IV	n.a.	< 0

Figure 12: Schematic behavior of R_W versus p_{WF_6}, divided by black dashed vertical lines into four zones of different reaction orders n_{H_2} and n_{WF_6}. The colored dashed vertical lines mark the repositioning of the zone transitions for changing T or p_{H_2}. In this sketch, the curves are based on equations only in the zones I – III.

Zone I. For $p_{WF_6} << p_{H_2}$, R_W increases linearly with p_{WF_6} [24, p.95], [29, 30]. Here the surface is saturated with H_2 so that n_{H_2} goes against zero and the incoming F atoms of each adsorbed WF_6 atom can be directly carried away by already on the surface dissociated H atoms [30, 42]. Thus WF_6 adsorption is the rate-limiting step.

Transition zone I $\rightarrow$ II. With increasing p_{WF_6} the amount of H on the surface is reduced continuously. Thus, near the transition for I $\rightarrow$ II, n_{WF_6} changes smoothly from 1 to 1/6 and n_{H_2} from 0 to 1/2 [29]. In fact, Creighton's investigations of the p_{H_2} dependence [30, Fig. 3] showed the existence of this transition with n_{H_2} values between 0 and 1/2 experimentally.

Zone II. The rate-limiting step in this zone is suggested to be HF desorption [18, 29] or the conversion of WF_4 to WF_3 [31].

Transition zone II $\rightarrow$ III. Finding the existence of the transition from zone II to III [Figure 9a, Figure 11] and a quantitative description [Equation 8, is a major outcome of the present article. However, it should be noted that the transition is in reality smoother than

it results from Equation 8 (s. Figure 9a). It is possible to smoothen the transition by using Equation 10.

$$R'_{sim} = \left(\frac{1}{[R_{\mathrm{WF}_6 dep.}]^m} + \frac{1}{[R_{\mathrm{WF}_6 indep.}]^m} \right)^{-1/m} \tag{10}$$

with $m = 1$ resulting in that R'_{sim} significantly underestimates R_{exp}, and with $m \to \infty$ resulting in that R'_{sim} converges to R_{sim} (Equation 8). A value in between would result in a better match. However, Equation 10 is not involved in the presented simulations, because it strongly increases the computational effort while having only a small influence on the results, and this only at the transition. In addition, more experimental data would be required first, to acquire a value for m.

Zone III. Most results in the literature and this work can be found for this zone with $n_{\mathrm{WF}_6} = 0$ and H_2 dissociation being the rate limiting step [23, 19, 20, 21, 22, 24]. The height and broadness of the plateau in Figure 12, as a function of T and p_{H_2}, is determined by the semi-empirical constants E_A and k_0. This zone provides typical and stable process conditions for ULSI technology without oversaturation of any of the species, so that R_{W} is least affected by depletion. Therefore, also pore infiltration processes, such as the synthesis of W_f/W, should be driven here, for the most possible uniform pore filling. With the help of the presented model $\dot{V}_{\mathrm{WF}_6}^{inlet}$ can be determined to be as low as possible, for lower production costs, and as high as necessary to safely stay in Zone III.

Zone IV. For p_{WF_6} higher than a value in between $p_{\mathrm{H}_2}/3$ and p_{H_2}, F becomes the majority surface species and hinders H_2 adsorption and dissociation, so that R_{W} decreases again [30, 31]. As shown by Creighton, this can lead to the extreme that R_{W} becomes even negative due to etching [30].

7. Simulation enhanced input for the Arrhenius plot

This section describes the procedure for obtaining the values for E_A and k_0, as they were given in Equation 8b. Generally, R_{W} data is needed together with its corresponding T and p_{H_2} data. For R_{W}, $R_{exp,max}$ along each fiber and tube were taken (Table 5, Table 6), since here, transient effects play a minor role, in contrast to the flanks of the R_{W}-curves. However, the corresponding T and p_{H_2} cannot be obtained trivially.

Step 1. As first estimation, T was set to T_H, and p_{H_2} was estimated via P_{tot} multiplied by $\dot{V}_{\mathrm{H}_2}^{inlet}$ divided by $\dot{V}_{tot}^{inlet}$. This data was used to create an Arrhenius plot ($\ln(R/p_{\mathrm{H}_2})$ vs. $1/T$) with two data points (fiber, tube) for each of the 15 process parameter sets. The result is shown together with literature data in Figure 13a. Using Python SciPy [43] for linear fitting, E_A results here in $(75.9 \pm 1.6)\,\mathrm{kJ/mol}$, and k_0 in $(10.34 \pm 1.08)\,\mu\mathrm{m\,s}^{-1}\mathrm{Pa}^{-1/2}$.

Step 2. The estimation of T and p_{H_2} at the position, where $R_{exp,max}$ was measured, can lead to large errors. For example, the T at the fiber surface of #1096 was significantly lower than T_H, due to convective cooling (similar to the final result, shown in Figure 7). Furthermore,

22

the p_{H_2} near the fiber and tube surface of #1101 was significantly lower than the p_{H_2} at the inlet, due to consumption (similar to Figure 8). Therefore, as next input for the Arrhenius plot, the estimated T and p_{H_2} were replaced by simulated values from the same location, at which the corresponding R_{sim} were maximal. However, changing E_A and k_0 as input for the simulation, results also in new values for the simulated T and p_{H_2}. This loop-dependence was solved iteratively. As convergence criterion was chosen that E_A remains constant in the tenths of a kJ/mol.

Step 3. The described procedure is for finding E_A and k_0 with respect to the case that R_W is independent of p_{WF_6} (zone III). However, for #1089, $R_{sim,max}$ did not match to $R_{WF_6 indep.,max.}$ (Equation 8b) but instead to $R_{WF_6 dep.,max.}$ (Equation 8a). Therefore, it must not be considered in the the Arrhenius plot and was filtered out. The final Arrhenius plot, resulting from a repeated iteration, is shown in Figure 13b. The R_W, T and p_{H_2} values used as input are provided in the appendix in Table 5 and Table 6. The resulting E_A of (73.7 ± 0.9) kJ/mol is similar to that of McConica [21], however, with a lower k_0 of $(38.22 \pm 4.85)\,\mu m\,s^{-1} Pa^{-1/2}$, so that the y values match to the results of Bryant [23] and Broadbent [19].
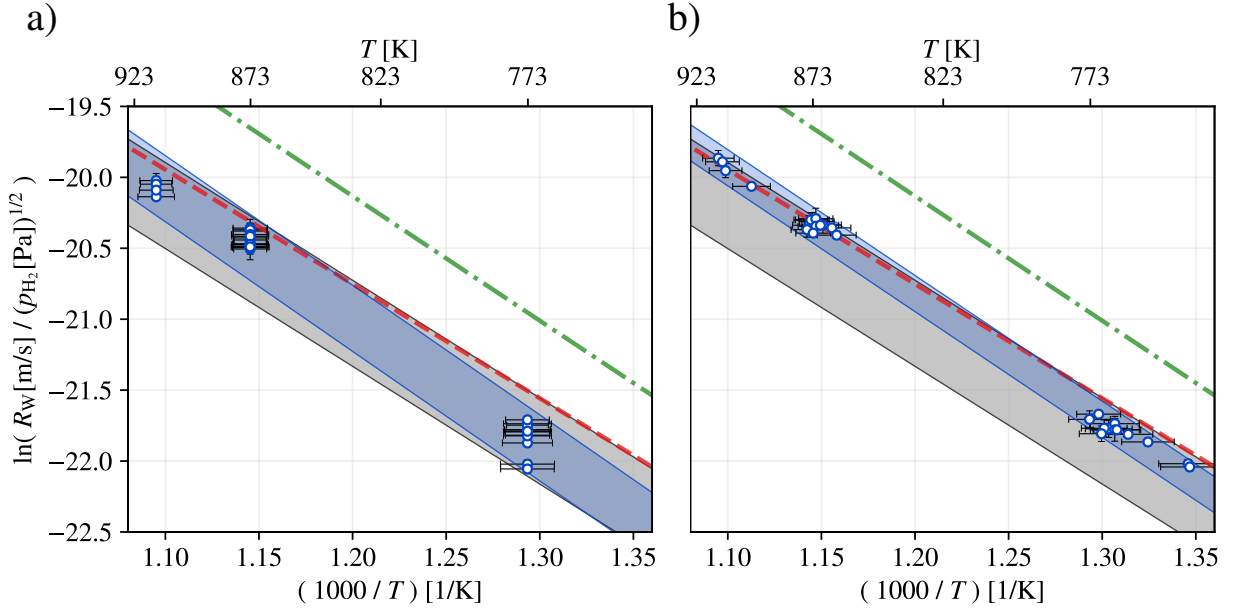

Figure 13: Arrhenius plots with linear fits (▭) to the data points (○), which result from $R_{exp,max}$ and further different input: a) $T = T_H$, and p_{H_2} estimated via inlet flow ratios, b) T and p_{H_2} taken from the simulation, where $R_{sim} = R_{sim,max}$, and using only the data being independent of p_{WF_6}. Literature data: —·— McConica [21], --- Bryant [23], ▬ Broadbent [19].

The changes in E_A and in the relative k_0 fitting error ($\Delta k_0/k_0$), resulting from the different Arrhenius plot inputs, are summarized in Table 4. $\Delta k_0/k_0$ gets significantly smaller due to the enhanced input from the iterative simulations (Step 2 and 3).

Table 4: Influence of different Arrhenius plot input on E_A and on the relative k_0 fitting error, as explained in the three steps in this section.

| | Input for | | | E_A | $\dfrac{\Delta k_0}{k_0}$ | |
Step	T	p_{H_2}	filter	[kJ/mol]	-	Fig.
1	T_H	inlet, estimated	none	75.9	0.23	13a
2	simulated at $R_{sim,max}$		none	72.8	0.18	
3	simulated at $R_{sim,max}$	p_{WF_6} indep.		**73.7**	**0.13**	13b

8. Summary and conclusions

The dependence of the W deposition rate (R_W) on the WF_6 partial pressure (p_{WF_6}) is discussed controversially in the literature. The experimental results and considerations of Van der Putte [27] and Creighton [30] indicated already that the p_{WF_6} dependence is determined by p_{WF_6} and p_{H_2}. However, no quantitative description was available. This is the gap of knowledge, which was addressed in this article. A new model was developed and validated by new experiments. For the commonly used case of H_2 overstoichiometry, the resulting rate equation describes well the most experimental data in the literature and all the data in this article.

The rate equation (Equation 8a) from McInerney et al. [29], which depends on p_{WF_6}, is found to be valid only at low p_{WF_6}. On the other hand, the commonly used rate equation, which is independent of p_{WF_6} (Equation 8b), is found to be valid only at higher p_{WF_6} (but $< 3\,p_{H_2}$). The transition location between the low and high p_{WF_6} regime depends mainly on the temperature (T) and negligible on p_{H_2}. This dependence can be included self-consistently by taking always the minimum of Equation 8a and Equation 8b, which describes the reaction limiting step. The resulting combined rate equation (Equation 8) was implemented in a transient 2D axial-symmetric COMSOL Multiphysics model, including the complex coupling of energy and mass transport phenomena with chemical reaction kinetics. In addition to the validation of R_W via optical microscopy, simulated T-profiles were validated by measuring near-surface T-profiles in high spatial resolution. Furthermore, the simulated partial pressures were validated indirectly via the WF_6 consumption rate, deduced from experimentally WF_6 flow rate and W mass gain measurements.

For the low p_{WF_6} regime, the semi-empirical constants E_A, k_1, and k_2 from Ref. [29] led to a good agreement. However, for the high p_{WF_6} regime, new values are suggested for E_A and k_0. By simulating T and p_{H_2} at the actual reaction location, the input for an Arrhenius plot was improved, which lowered the fitting error significantly. In this way, E_A and k_0 resulted in $(73.7 \pm 0.9)\,\text{kJ/mol}$ and $(38.22 \pm 4.85)\,\mu\text{m}\,\text{s}^{-1}\text{Pa}^{-1/2}$, respectively.

The new rate equation, presented and validated in this article, makes it possible to predict R_W quantitatively as function of T, p_{H_2} and p_{WF_6} for a much larger p_{WF_6} range compared to what was previously available in the literature. This is particularly necessary to comprehensively model the production of W_f/W, since here, p_{WF_6} should start high, but

eventually decreases to zero within the pore structure.

9. Acknowledgments

10. Appendix

Table 5: Inside the **steel tube**: $R_{exp,max}$, $R_{sim,max}$, and T and p_i at $R_{sim,max}$.

ID	$R_{exp,max}$ [nm/s]	$R_{sim,max}$ [nm/s]	$T@R_{sim,max}$ [K]	$p_{H_2}@R_{sim,max}$ [kPa]	$p_{WF_6}@R_{sim,max}$ [kPa]
1086	121.7 ± 8.4	125.1 ± 8.3	874.6 ± 6.6	6.85 ± 0.16	0.51 ± 0.06
1088	62.5 ± 3.3	66.9 ± 5.8	875.4 ± 6.5	1.92 ± 0.03	0.19 ± 0.0
1089	28.8 ± 2.3	32.3 ± 4.8	874.7 ± 6.6	0.56 ± 0.07	0.06 ± 0.01
1090	139.4 ± 5.1	134.4 ± 11.1	871.4 ± 6.9	8.52 ± 0.01	0.35 ± 0.02
1091	133.2 ± 7.0	129.8 ± 9.9	873.3 ± 6.8	7.61 ± 0.07	0.73 ± 0.04
1092	120.7 ± 6.4	118.4 ± 8.2	873.9 ± 6.8	6.25 ± 0.14	1.36 ± 0.05
1093	127.6 ± 9.8	121.1 ± 9.5	871.8 ± 6.9	6.86 ± 0.06	1.58 ± 0.03
1094	189.5 ± 9.7	196.7 ± 15.0	910.1 ± 7.2	7.69 ± 0.05	0.75 ± 0.03
1095	24.5 ± 1.5	25.6 ± 3.1	767.2 ± 7.3	4.91 ± 0.07	0.6 ± 0.01
1096	18.1 ± 1.0	17.7 ± 2.4	765.3 ± 7.6	2.49 ± 0.07	0.62 ± 0.02
1097	34.8 ± 2.1	36.8 ± 4.2	768.6 ± 7.1	9.77 ± 0.06	0.56 ± 0.0
1098	33.4 ± 1.9	37.3 ± 4.2	769.5 ± 7.0	9.78 ± 0.06	0.15 ± 0.01
1099	34.2 ± 2.9	34.9 ± 4.3	765.3 ± 7.6	9.7 ± 0.03	2.41 ± 0.0
1100	33.9 ± 2.1	36.2 ± 3.6	773.3 ± 6.6	8.21 ± 0.02	0.9 ± 0.02
1101	185.2 ± 10.3	182.3 ± 10.4	913.3 ± 7.0	6.16 ± 0.21	0.34 ± 0.08

Table 6: At the **W fiber**: $R_{exp,max}$, $R_{sim,max}$, and T and p_i at $R_{sim,max}$.

ID	$R_{exp,max}$ [nm/s]	$R_{sim,max}$ [nm/s]	$T@R_{sim,max}$ [K]	$p_{H_2}@R_{sim,max}$ [kPa]	$p_{WF_6}@R_{sim,max}$ [kPa]
1086	120.4 ± 3.4	120.9 ± 8.7	871.8 ± 7.2	6.79 ± 0.18	0.58 ± 0.05
1088	60.9 ± 1.9	65.1 ± 6.1	872.9 ± 7.0	1.92 ± 0.03	0.2 ± 0.0
1089	29.1 ± 1.0	31.5 ± 4.9	872.2 ± 7.1	0.56 ± 0.07	0.06 ± 0.01
1090	133.1 ± 2.5	125.3 ± 11.4	865.3 ± 7.5	8.51 ± 0.02	0.4 ± 0.02
1091	128.3 ± 3.1	123.4 ± 10.3	869.0 ± 7.4	7.57 ± 0.09	0.79 ± 0.03
1092	115.3 ± 3.0	112.5 ± 8.6	870.0 ± 7.4	6.15 ± 0.16	1.42 ± 0.05
1093	113.0 ± 3.0	109.5 ± 9.7	863.4 ± 7.7	6.79 ± 0.08	1.62 ± 0.03
1094	169.1 ± 4.0	173.9 ± 15.2	898.7 ± 8.0	7.64 ± 0.07	0.82 ± 0.03
1095	22.4 ± 0.6	21.2 ± 3.0	755.0 ± 7.9	4.92 ± 0.07	0.6 ± 0.01
1096	13.6 ± 0.4	12.5 ± 2.0	743.0 ± 8.5	2.48 ± 0.07	0.62 ± 0.02
1097	33.3 ± 0.7	32.9 ± 4.1	761.1 ± 7.6	9.78 ± 0.05	0.58 ± 0.0
1098	34.4 ± 0.8	34.7 ± 4.2	764.6 ± 7.4	9.79 ± 0.06	0.17 ± 0.01
1099	26.4 ± 0.8	24.5 ± 3.6	742.5 ± 8.5	9.72 ± 0.03	2.42 ± 0.01
1100	35.2 ± 0.9	34.7 ± 3.7	770.4 ± 6.9	8.22 ± 0.02	0.92 ± 0.02
1101	177.5 ± 4.3	176.2 ± 10.8	911.5 ± 7.4	5.96 ± 0.22	0.43 ± 0.07

Table 7: Material and species properties used in the model, formated for copy-paste

magnitude;[unit];	species;	value;	reference
density ρ;[kg/m^3];	W(s);	19 250;	[25, 26]
density ρ^0;[kg/m^3];	WF6(g);	12.4;	[32]
dipol moment μ_D;[D];	H2(g);	0;	not polar
dipol moment μ_D;[D];	HF(g);	1.826178;	[44]
dipol moment μ_D;[D];	WF6(g);	0;	not polar
emissivity ϵ_{rad};[-];	Steel 1.4571;	0.35;	intern
emissivity ϵ_{rad};[-];	W(s);	0.3±0.1;	intern
heat capacity c_p;[J/mol/K];	H2(g);	(3.300+2.231e-4*T+9.555e-8*T^2+3.143e1/T)*R;	fit to [35]
heat capacity c_p;[J/mol/K];	WF6(g);	(2.167e1-1.510e-3*T+3.079e-7*T^2-2.069e3/T)*R;	fit to [35]
heat capacity c_p;[J/mol/K];	HF(g);	(3.080+4.544e-4*T+1.990e-8*T^2+8.849e1/T)*R;	fit to [35]
heat capacity c_p;[J/mol/K];	W(s);	(2.882+4.094e-4*T+4.918e-8*T^2-2.514e1/T)*R;	fit to [35]
heat capacity c_p;[J/kg/K)];	Steel 1.4571;	500;	[45]
molar enthalpy h;[J/mol];	H2(g);	(3.450e-3+1.258e-8/2*T+5.657e-11/3*T^2-1.030/T)*RT;	fit to [35]
molar enthalpy h;[J/mol];	WF6(g);	(1.417e-2+3.152e-6/2*T-7.055e-10/3*T^2-2.116e2/T)*RT;	fit to [35]
molar enthalpy h;[J/mol];	HF(g);	(3.434e-3+2.377e-8/2*T+5.261e-11/3*T^2-3.381e1/T)*RT;	fit to [35]
molar enthalpy h;[J/mol];	W(s);	(2.793e-3+2.509e-7/2*T+6.878e-12/3*T^2-8.554e-1/T)*RT;	fit to [35]
molar entropie s;[J/mol/K];	H2(g);	(3.490*ln(T)-6.012e-5*T+1.043e-7/2*T^2-4.156)*R;	fit to [35]
molar entropie s;[J/mol/K];	WF6(g);	(1.312e1*ln(T)+8.529e-3*T-1.565e-6/2*T^2-3.618e1)*R;	fit to [35]
molar entropie s;[J/mol/K];	HF(g);	(3.498*ln(T)-8.707e-5*T+1.096e-7/2*T^2+9.911e-1)*R;	fit to [35]
molar entropie s;[J/mol/K];	W(s);	(2.788*ln(T)+5.122e-4*T+7.961e-9/2*T^2-1.211e1)*R;	fit to [35]
potential characteristic lengths σ;[Å];	H2(g);	2.827;	[36]
potential characteristic lengths σ;[Å];	HF(g);	3.148;	[46]
potential characteristic lengths σ;[Å];	WF6(g);	4.973+9.284e-4*T+6.582e-7*T^2-7.315e-10*T^3;	[47]
potential energy minimum ϵ/k_B;[K];	H2(g);	59.7;	[24]
potential energy minimum ϵ/k_B;[K];	HF(g);	330;	[46]
potential energy minimum ϵ/k_B;[K];	WF6(g);	819.9-1.06*T+6.19e-4*T^2-6.62e-8*T^3;	[47]
thermal conductivity k;[W/m/K];	Steel 1.4571;	11.3+0.0127*T;	intern
thermal conductivity k;[W/m/K];	W(s);	207.24-0.269*(T+273)+3e-4*(T+273)^2+1e-7*(T+273)^3;	[25]

References

[1] F. Romanelli, Fusion Electricity a roadmap to the realisation of fusion energy, European Fusion Development Agreement, EFDA, 2012, ISBN 978-3-00-040720-8.

[2] H. Zohm, Assessment of DEMO challenges in technology and physics, Fusion Engineering and Design 88 (6-8) (2013) 428–433.

[3] R. Wenninger, M. Bernert, T. Eich, E. Fable, G. Federici, A. Kallenbach, A. Loarte, C. Lowry, D. McDonald, R. Neu, T. Pütterich, P. Schneider, B. Sieglin, G. Strohmayer, F. Reimold, M. Wischmeier, DEMO divertor limitations during and in between ELMs, Nuclear Fusion 54 (11) (2014) 114003.

[4] G. Federici, G. Giruzzi, C. Lowry, R. Kemp, D. Ward, R. Wenninger, H. Zohm, EU DEMO design and R&D studies, in: Fusion Engineering (SOFT), 2013 IEEE 25th Symposium on Fusion Technology, 2013, pp. 1–8.

[5] J. W. Coenen, S. Antusch, M. Aumann, W. Biel, J. Du, J. Engels, S. Heuer, A. Houben, T. Hoeschen, B. Jasper, et al., Materials for DEMO and reactor applications – boundary conditions and new concepts, Physica Scripta 2016 (T167).

[6] J. W. Coenen, Y. Mao, S. Sistla, J. Riesch, T. Hoeschen, C. Broeckmann, R. Neu, Ch. Linsmeier, Improved pseudo-ductile behavior of powder metallurgical tungsten short fiber-reinforced tungsten (W_f/W), Nuclear Materials and Energy 15 (2018) 214–219.

[7] Y. Mao, J. W. Coenen, J. Riesch, S. Sistla, J. Almanstötter, B. Jasper, A. Terra, T. Höschen, H. Gietl, M. Bram, et al., Development and characterization of powder metallurgically produced discontinuous tungsten fiber reinforced tungsten composites, Physica Scripta 2017 (T170) (2017) 014005.

[8] Y. Mao, J. W. Coenen, J. Riesch, S. Sistla, J. Almanstötter, B. Jasper, A. Terra, T. Höschen, H. Gietl, Ch. Linsmeier, C. Broeckmann, Influence of the interface strength on the mechanical properties of discontinuous tungsten fiber-reinforced tungsten composites produced by field assisted sintering technology, Composites Part A: Applied Science and Manufacturing 107 (2018) 342–353.

[9] J. Riesch, J.-Y. Buffiere, T. Höschen, M. di Michiel, M. Scheel, Ch. Linsmeier, J.-H. You, In situ synchrotron tomography estimation of toughening effect by semi-ductile fibre reinforcement in a tungsten-fibre-reinforced tungsten composite system, Acta Materialia 61 (19) (2013) 7060–7071.

[10] J. Riesch, M. Aumann, J. W. Coenen, H. Gietl, G. Holzner, T. Höschen, P. Huber, M. Li, Ch. Linsmeier, R. Neu, Chemically deposited tungsten fibre-reinforced tungsten - The way to a mock-up for divertor applications, Nuclear Materials and Energy (2016) –ICFRM Conference 2015.

[11] J. Riesch, Y. Han, J. Almanstötter, J. W. Coenen, T. Höschen, B. Jasper, P. Zhao, Ch. Linsmeier, R. Neu, Development of tungsten fibre-reinforced tungsten composites towards their use in DEMO - potassium doped tungsten wire, Physica Scripta 2016 (T167) (2016) 014006.

[12] A. F. Zinn, The Chemistry of Metal CVD, VCH Verlagsgesellschaft, Weinheim, 2007, Chapt. Chemical vapor deposition of tungsten, pp. 105–174.

[13] N. E. Miller, I. Beinglass, CVD tungsten interconnect and contact barrier technology for VLSI, Solid State Technology 25 (12) (1982) 85–90.

[14] E. Granneman, Thin films in the integrated circuit industry: requirements and deposition methods, Thin Solid Films 228 (1-2) (1993) 1–11.

[15] K. Kuijlaars, C. Kleijn, H. van Den Akker, A detailed model for low-pressure CVD of tungsten, Thin Solid Films 270 (1-2) (1995) 456–461.

[16] K. Kuijlaars, C. Kleijn, H. Van den Akker, Simulation of selective tungsten chemical vapour deposition, Materials Science in Semiconductor Processing 1 (1) (1998) 43–54.

[17] C. Kleijn, R. Dorsman, K. Kuijlaars, M. Okkerse, H. Van Santen, Multi-scale modeling of chemical vapor deposition processes for thin film technology, Journal of Crystal Growth 303 (1) (2007) 362–380.

[18] T. Oosterlaken, G. Leusink, G. Janssen, S. Radelaar, The hydrogen reduction of WF_6: A kinetic study based on in situ partial pressure measurements, Journal of the Electrochemical Society 143 (5) (1996) 1668–1675.

[19] E. K. Broadbent, Selective Low Pressure Chemical Vapor Deposition of Tungsten, Journal of The Electrochemical Society 131 (6) (1984) 1427.

[20] Y. Pauleau, Kinetics and Mechanism of Selective Tungsten Deposition by LPCVD, Journal of the Electrochemical Society 132 (11) (1985) 2779.

[21] C. M. McConica, K. Krishnamani, The Kinetics of LPCVD Tungsten Deposition in a Single Wafer Reactor, J. Electrochem. Soc. 133 (1986) 2542–2548.

[22] H. Körner, Selective low pressure chemical vapour deposition of tungsten: Deposition kinetics, selectivity and film properties, Thin Solid Films 175 (1989) 55–60.

[23] W. Bryant, Kinetics of Tungsten Deposition by the Reaction of WF_6 and Hydrogen, Journal of The Electrochemical Society 125 (9) (1978) 1534.

[24] C. R. Kleijn, C. Werner, Modeling of chemical vapor deposition of tungsten films, Birkhäuser, Basel, 1993.

[25] Y. Lian, X. Liu, Z. Xu, J. Song, Y. Yu, Preparation and properties of CVD-W coated W/Cu FGM mock-ups, Fusion Engineering and Design 88 (9/10) (2013) 1694–1698.

[26] F. Hamelmann, G. Haindl, A. Aschentrup, A. Klipp, U. Kleineberg, P. Jutzi, U. Heinzmann, Plasma enhanced MOCVD of smooth nanometer-sized Metal/Silicon Single- and multilayer films, in: T. Allendorf, M.D.; Besman (Ed.), CVD XV: Proceedings of the Fifteenth International Symposium on Chemical Vapor Deposition, Vol. 2000, The Electrochemical Society, 2000, p. 131.

[27] P. Van der Putte, The reaction kinetics of the H_2 reduction of WF_6 in the chemical vapor deposition of tungsten films, Philips Journal of Research 42 (5/6) (1987) 608–626.

[28] W. Bryant, G. Meier, Kinetics of the Chemical Vapor Deposition of Tungsten, J. Electrochem. Soc. 120.

[29] E. J. McInerney, E. Srinivasan, D. C. Smith, G. Ramanath, Kinetic rate expression for tungsten chemical vapor deposition in different WF_6 flow regimes from step coverage measurements, Zeitschrift für Metallkunde 91 (2000) 573–580.

[30] J. Creighton, The surface chemistry and kinetics of tungsten chemical vapor deposition and selectivity loss, Thin Solid Films 241 (1-2) (1994) 310–317.

[31] R. Arora, R. Pollard, A Mathematical Model for Chemical Vapor Deposition Processes Influenced by Surface Reaction Kinetics: Application to Low-Pressure Deposition of Tungsten, Journal of The Electrochemical Society 138 (5) (1991) 1523–1537.

[32] Institut für Arbeitsschutz der Deutschen Gesetzlichen Unfallversicherung, GESTIS-Stoffdatenbank WF_6 (2019).

[33] COMSOL INC. url: https://www.comsol.com/.

[34] P. A. Tipler, Physik, 3rd Edition, Spektrum Akademischer Verlag GmbH, Heidelberg, 2000

[35] I. Barin (Ed.), Thermochemical Data of Pure Substances, VCH Verlagsgesellschaft, Weinheim, 1995.

[36] J. O. Hirschfelder, C. F. Curtiss, R. B. Bird, The Molecular Theory of Gases and Liquids, John Wiley & Sons Inc, New York, 1964.

[37] D. F. Fairbanks, C. R. Wilke, Diffusion Coefficients in Multicomponent Gas Mixtures, Industrial & Engineering Chemistry 42 (3) (1950) 471–475.

[38] C. R. Wilke, C. Y. Lee, Estimation of Diffusion Coefficients for Gases and Vapors, Industrial & Engineering Chemistry 47 (6) (1955) 1253–1257.

[39] K. Kuijlaars, C. Kleijn, H. Van Den Akker, Multi-component diffusion phenomena in multiple-wafer chemical vapour deposition reactors, The Chemical Engineering Journal and The Biochemical Engineering Journal 57 (2) (1995) 127–136.

[40] C. R. Kleijn, A. Hasper, J. Holleman, C. J. Hoogendoorn, J. Middelhoek, An Experimental and Modeling Study of the Tungsten LPCVD Growth Kinetics from H_2-WF_6 at Low WF_6 Partial Pressures, in: S. S. Wong, S. Furukawa (Eds.), Tungsten and Other Advanced Metals for VLSI/ULSI Applications V, MRS Pub., 1990, pp. 109–116.

[41] A. Hasper, Modeling and Optimization of the Step Coverage of Tungsten LPCVD in Trenches and Contact Holes, Journal of The Electrochemical Society 138 (6) (1991) 1728.

[42] M. Li, S. Dew, M. Brett, T. Smy, Kinetic simulation of metal chemical-vapor deposition on high aspect ratio features in modern very-large-scale-integrated processing, Journal of Vacuum Science & Technology B: Microelectronics and Nanometer Structures Processing, Measurement, and Phenomena

18 (3) (2000) 1343–1347.

[43] Python library. url: https://docs.scipy.org/doc/scipy/reference/generated/scipy.optimize.curve_fit.html.

[44] J. Rumble (Ed.), CRC Handbook of Chemistry and Physics, 99th Edition, CRC Press, Boca Raton, 2018.

[45] Deutsche Edelstahlwerke, Werkstoffdatenblatt X6CrNiMoTi17-12-2, 1.4571 (2015).

[46] F. M. Mourits, F. H. Rummens, A critical evaluation of Lennard–Jones and Stockmayer potential parameters and of some correlation methods, Canadian Journal of Chemistry 55 (16) (1977) 3007–3020.

[47] L. Zarkova, U. Hohm, pVT–Second Virial Coefficients B(T), Viscosity η(T), and Self-Diffusion ρD(T) of the Gases: BF_3, CF_4, SiF_4, CCl_4, $SiCl_4$, SF_6, MoF_6, WF_6, UF_6, $C(CH_3)_4$, and $Si(CH_3)_4$ Determined by Means of an Isotropic Temperature-Dependent Potential, Journal of Physical and Chemical Reference Data 31 (1) (2002) 183–216.